APPLIED SCIENCES AND ENGINEERING

Printed multifunctional flexible device with an integrated motion sensor for health care monitoring

Yuki Yamamoto,* Shingo Harada,* Daisuke Yamamoto, Wataru Honda, Takayuki Arie, Seiji Akita, Kuniharu Takei[†]

Real-time health care monitoring may enable prediction and prevention of disease or improve treatment by diagnosing illnesses in the early stages. Wearable, comfortable, sensing devices are required to allow continuous monitoring of a person's health; other important considerations for this technology are device flexibility, low-cost components and processing, and multifunctionality. To address these criteria, we present a flexible, multifunctional printed health care sensor equipped with a three-axis acceleration sensor to monitor physical movement and motion. Because the device is designed to be attached directly onto the skin, it has a modular design with two detachable components: One device component is nondisposable, whereas the other one is disposable and designed to be worn in contact with the skin. The design of this disposable sensing sheet takes into account hygiene concerns and low-cost materials and fabrication methods as well as features integrated, printed sensors to monitor for temperature, acceleration, electrocardiograms, and a kirigami structure, which allows for stretching on skin. The reusable component of the device contains more expensive device components, features an ultraviolet light sensor that is controlled by carbon nanotube thin-film transistors, and has a mechanically flexible and stable liquid metal contact for connection to the disposable sensing sheet. After characterizing the electrical properties of the transistors and flexible sensors, we demonstrate a proof-of-concept device that is capable of health care monitoring combined with detection of physical activity, showing that this device provides an excellent platform for the development of commercially viable, wearable health care monitors.

INTRODUCTION

Continuous monitoring of a person's health data, such as heart rate, body temperature, and blood pressure, would assist medical health care providers in early prediction and diagnosis of adverse conditions or diseases, allowing patients to be treated more quickly and effectively, thereby decreasing patient numbers and medical costs in the long term. To enable this, health monitoring sensors should be worn by people throughout the day (including during sleep), allowing a continuous collation of health data. In this regard, comfort is a key consideration in the device design. Mechanically flexible devices are ideal candidates for wearable health care sensors and have been widely studied. Various material platforms and structures have been reported for health care monitoring devices (1), such as temperature sensors (2, 3), electrocardiogram (ECG) sensors (4, 5), heartbeat sensors (6, 7), chemical sensors (8, 9), and drug delivery systems (10, 11), and multifunctional sensing has been used not only for health care monitoring but also for diverse applications (10, 12, 13). Although monitoring health conditions is valuable, simultaneous monitoring of physical activity would provide some much-needed context to the data, considering that vital signs, such as skin temperature and ECG, strongly depend on activity and that real-time health information alone is not completely sufficient for a full analysis of the wearer's condition or for the prediction or diagnosis of disease. Although there have been several reports of sensors and actuators for this type of application (2–11, 14–16), neither printed nor flexible acceleration (motion) sensors have been demonstrated to date. Note that strain sensors have been used to monitor human motion through attachment to joints (17, 18). However, these can only monitor the motion of the joints,

Department of Physics and Electronics, Osaka Prefecture University, Sakai, Osaka 599-8531, Japan.
*These authors contributed equally to this work.
†Corresponding author. Email: takei@pe.osakafu-u.ac.jp

which is not always representative of the full range of human motion and activity. Accurate motion data collection from these devices presents a challenge because inflexible acceleration sensors, like those currently used in conventional (that is, nonflexible) wearable devices, need to be integrated onto flexible substrates with other health monitoring sensors. Another challenge is to design low-cost devices, allowing widespread usage and availability to the general public. Hence, it is important to strike a balance between device cost and functionality.

To address these challenges, we report a proof-of-concept, flexible, wearable health care monitoring device, which features a detachable multilayered design, a printed three-axis acceleration sensor for motion detection, and three separate sensors for monitoring vital signs. Notably, we have designed the devices to use carbon nanotube (CNT)–based sensors and transistors, which exploit the unique and high-performance properties of these materials, such as high mobility. Three printed health monitoring components are used: a skin temperature sensor, an ECG sensor, and an environmental sensor for detecting environmental ultraviolet (UV) light. Note that UV sensing cannot be used effectively in tandem with ECG monitoring because the device must be worn underneath clothes for effective monitoring of the latter. Hence, the purpose of the UV sensor in this study is to demonstrate the possibility of multifunctional sensor integration. Moreover, the monitoring of sunlight exposure may be applicable to other wearable devices, such as tracking devices, which are typically worn on the arm or wrist. Flexible transistors are also integrated for the switching of the sensors. The device features two detachable components (19, 20) that address cost and hygiene concerns. A nondisposable sensor sheet carries higher-cost components, whereas a disposable sensor sheet designed to be worn in contact with the skin is designed and fabricated with low cost in mind. The two sheets are attached via a flexible, stable, eutectic gallium-indium (EGaIn) liquid metal contact (21). Finally, to demonstrate the suitability of these devices for health care monitoring, we monitored simultaneous skin

temperature, ECG, and UV exposure in tandem with real-time motion sensing under different states of physical activity, including walking, running, and sleeping.

RESULTS

The device consists of two sheets, as shown in Fig. 1 (A to C) and fig. S1. The fabrication process is explained in detail in Materials and Methods. The disposable sensing component for direct contact with the skin features a three-axis acceleration sensor, an ECG sensor, and a temperature sensor with a silver (Ag) interconnection, all of which were printed on a disposable polyethylene terephthalate (PET) sheet with a kirigami structure (22), allowing it to stretch comfortably on the

human body. The multilayer plastic sheets of the kirigami structure suppress its mechanical rigidity, rendering it unable to fully stretch after the device is attached to skin. However, when the wearer is active, the device can stretch slightly due to the dynamic between the kirigami structure and skin in motion. Although the device is not entirely stretchable, the kirigami structure improves the comfort for wearers. We also note that the kirigami structure was made to prevent the mechanical and electrical failures based on the stress caused by mechanical stretching, particularly where the device includes sensors and thin-film transistors (TFTs). In the future, electrodes will likely need to be formed over the structure. To confirm this possibility, we measured the electrical resistance change of printed Ag electrodes over the structure as a function of stretchability. Figure S2 shows that
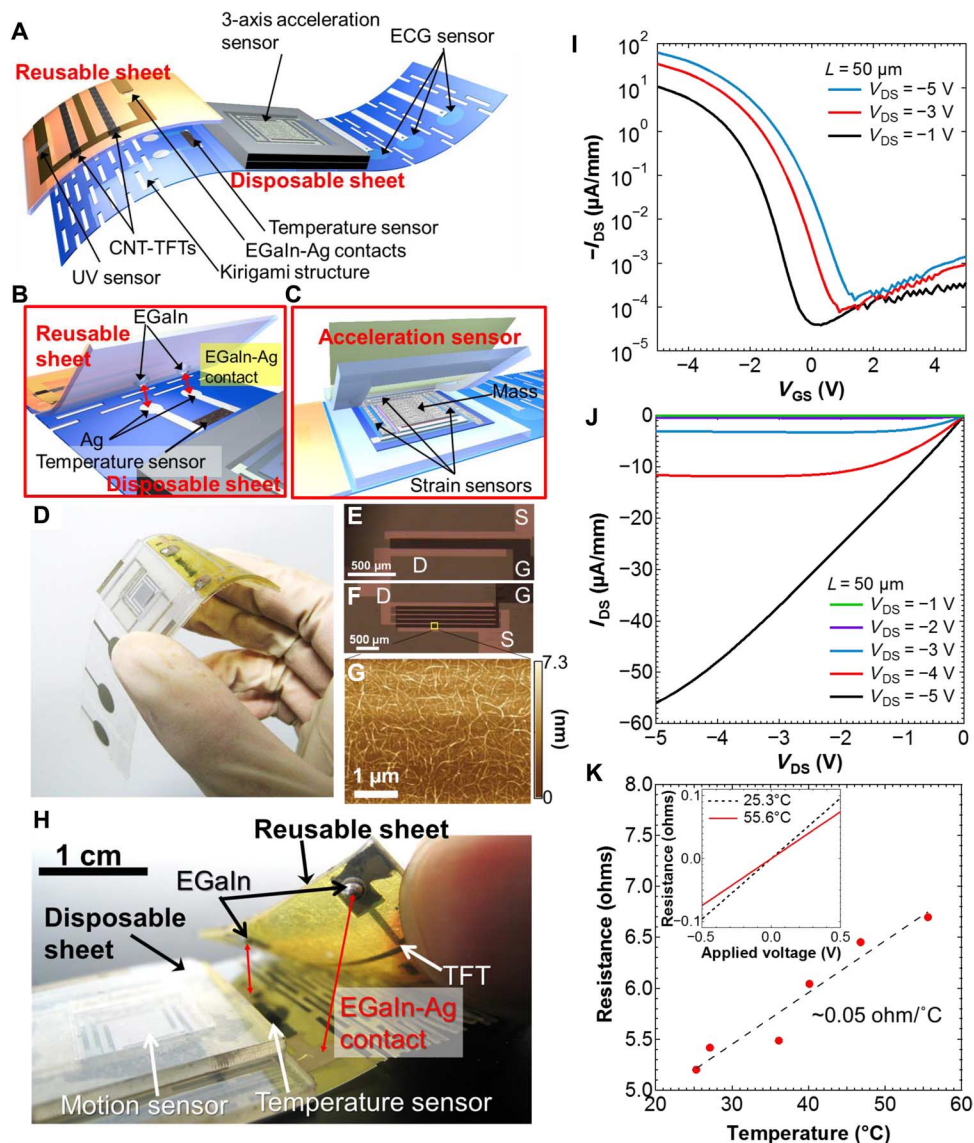

Fig. 1. Multifunctional, flexible, wearable health monitoring patch. Schematics of (**A**) the whole device structure, including both disposable and reusable components, (**B**) EGaIn and Ag contact region between the sheets, (**C**) and three-axis acceleration sensor. (**D**) Image of the fabricated device. Optical microscopy images showing the CNT-TFT architectures used for (**E**) the UV sensor and (**F**) the temperature sensor. (**G**) Atomic force microscopy image of the CNT network film used for the TFT semiconductor channel. (**H**) Image of the device, particularly focused on the EGaIn-Ag contact region between the sheets. I_{DS}-V_{GS} (**I**) and I_{DS}-V_{DS} (**J**) characteristics of a CNT-TFT representative of the devices used in this study. (**K**) Plot of electrical resistance as a function of temperature for the EGaIn-Ag contact. The inset compares I-V characteristics at 25.3°C and 55.6°C.

the resistance was increased slightly up to 2.6% when the substrate was stretched to 100%. Because the electrode resistance is ~6.12 ohms, a few percent resistance change is negligible for sensor integration, where sensor resistance is much higher than this value. The second component is a reusable sheet based on a polyimide substrate consisting of a UV sensor, CNT-TFT–mediated switching circuits for the sensors on both sheets, and a fixed EGaIn electrical connection. The electrical interface between the two sheets connects the temperature sensor on the disposable component to the CNT-TFT circuit on the reusable sheet. This was made using EGaIn contacts, which have previously been reported to be stable under mechanical bending (19). The EGaIn was placed on the reusable sheet in small chambers made of a silicone rubber and polydimethylsiloxane (PDMS), as described in Fig. 1B and fig. S3. All sensors were fabricated by solution-based techniques, such as a screen printing. The sensors operate through resistance changes induced in response to the respective stimuli. The acceleration sensor has three strain sensors, which respond to changes in structural strain. These strain sensors were fabricated from a mixture of Ag nanoparticles (NPs) and single-walled CNT inks. The temperature sensor was printed from a mixture of CNT ink and poly(3,4-ethylenedioxythiophene):polystyrene sulfonate (PEDOT: PSS) solution. Last, the UV sensor was fabricated through the deposition of ZnO nanowire networks. Images of the entire device and its individual components are presented in Fig. 1D and fig. S4.

The channel width (W) and length (L) of CNT-TFTs were chosen such that their resistance characteristics match those of the UV and temperature sensors. These values (W/L) are 1 mm/100 μm and 10 mm/50 μm, respectively (Fig. 1, E and F). The morphology of a typical CNT network used for these TFTs is shown in the atomic force microscopy image in Fig. 1G. The measurement indicates that the CNT layer has a relatively high-density, uniform network, which is required for reliable, high-performance TFTs. The representative electrical properties of the CNT-TFTs are shown in Fig. 1 (I and J), with a measured field-effect mobility and I_{on}/I_{off} ratio of ~5.8 cm²/Vs and ~10^5, respectively. The mobility fabricated in this study is low compared to other reports (23) because the density of the CNT network is low, as shown in Fig. 1G. However, by sacrificing the mobility, I_{on}/I_{off} ratio is high, which is appropriate for the switching functions that are used in this study. The relationship between mobility and I_{on}/I_{off} ratio agrees with previous reports. The flexible EGaIn-Ag electrical contact between the disposable and reusable sheets is a unique design feature of this device and is shown pictorially in Fig. 1H and fig. S3. The electrical resistance of the EGaIn-Ag contact and Ag electrode is ~5.2 ohms at 25.3°C, which increases at a rate of ~0.05 ohm/°C, as shown in Fig. 1K. Despite this increased resistance with temperature, the overall resistance of the EGaIn-Ag interconnection is low enough to enable precise measurement of the sensor output, considering that the resistance of the sensing components is much higher: ~3.36 kilohms per square for the temperature sensor and ~17.1 megohms per square for the UV sensor under illumination. Even under human motion, electrical resistance change between the EGaIn-Ag electrodes was less than 0.1 ohm, suggesting that this contact is electrically stable for wearable device application (fig. S5).

As previously mentioned, physical activity data provide important context for vital sign data recorded by wearable monitoring devices, considering that different degrees of activity strongly affect conditions, such as ECG and body temperature. The printed three-axis acceleration sensor used to measure this activity consists of four beams integrated with three resistive strain sensors and an Ag electrode, as shown in Fig. 2 (A and B), and operates by measuring the deformation of the beams in response to external acceleration. By attaching an acrylic plate (weight = 38 mg) as a mass, as illustrated in Fig. 2C, a strain distribution is induced in the sensor, which is dependent on the acceleration force and direction (for further structural detail, see fig. S6 and the Supplementary Materials). Figure 2 (D and E) depicts the stress distributions calculated by finite element method (FEM) simulations when accelerations of 20 m/s² are applied in the z and y axes. These data suggest that the changes in stress value in the strain sensor (for example, sensors #1 and #2 in Fig. 2) depend on the direction of acceleration. By reading the distributions of stress/strain and their magnitude, the corresponding direction and magnitude of acceleration can be readily determined.

First, the frequency dependence of sensor #1 (as shown in Fig. 2B) was evaluated at ~25 m/s² z-axis acceleration. The results are presented in Fig. 2F and fig. S7. Considering that the device is designed to monitor human motion, an acceleration frequency range of 1 to 6 Hz was chosen to test the sensor. On acceleration, vibration was observed with a duration of around 0.3 s. Because of this vibration, the precise acceleration measurement should be less than 4 Hz. However, by observing the peak value of the resistance change, it is possible to extract the measurement of motion at around 6 Hz, as shown in fig. S7. Note that positive and negative accelerations (~±25 m/s²) were applied in about 50 ms because of the measurement setup for frequency dependence measurements. Although these positive and negative accelerations were applied, because of much faster duration of acceleration than the vibration of the sensor (~0.3 s), the effect of the negative acceleration is almost negligible in terms of the maximum resistance change confirmed by comparing this to results at only positive acceleration applied to the acceleration sensor. As the simulation in Fig. 2E shows, when y-axis acceleration is applied, almost no strain is detected by the sensor #2 beam. Correspondingly, there is almost no strain in the sensor #1 beam when x-axis acceleration is applied because of the symmetric structure. The experimental results presented in fig. S7 agree with the strain distribution and magnitude extracted from the FEM simulation. Although there are some variations in the resistance change, the change in output resistance displays sufficient independence from the acceleration frequency for frequencies up to 6 Hz (Fig. 2G).

Second, the sensitivity of acceleration sensing was evaluated by applying different acceleration amplitudes to each axis of sensor #1 (these measurements were conducted on this sensor only). As shown in Fig. 2 (H and I), the threshold acceleration was observed to be around 5 to 12 m/s², depending on the direction of acceleration, except for the x axis. After this point, the change in resistance increased in a near-linear fashion with increasing acceleration. The post-threshold sensitivities extracted from the linear fitting of z, y, and x axes are 0.064, 0.057, and 0.00% m⁻¹ s² $m^{-1} s^2$, respectively. When acceleration in the opposite direction (that is, negative acceleration shown in Fig. 2, H and I) was applied, maximum resistance change ($R - R_0$, where R_0 and R are resistances before and after acceleration, respectively) was negative, corresponding to the fact that the resistance at certain negative acceleration was decreased, whereas it was positive change at the positive acceleration for z-axis acceleration. For x and y axes, because of high noise and small resistance change below 25 m/s² used in this study, no significant change was observed when the negative acceleration was applied (Fig. 2H). On the basis of the FEM simulation, the maximum stress on the beam changes linearly as a function of acceleration, as plotted in Fig. 2I. Based on both experimental and FEM
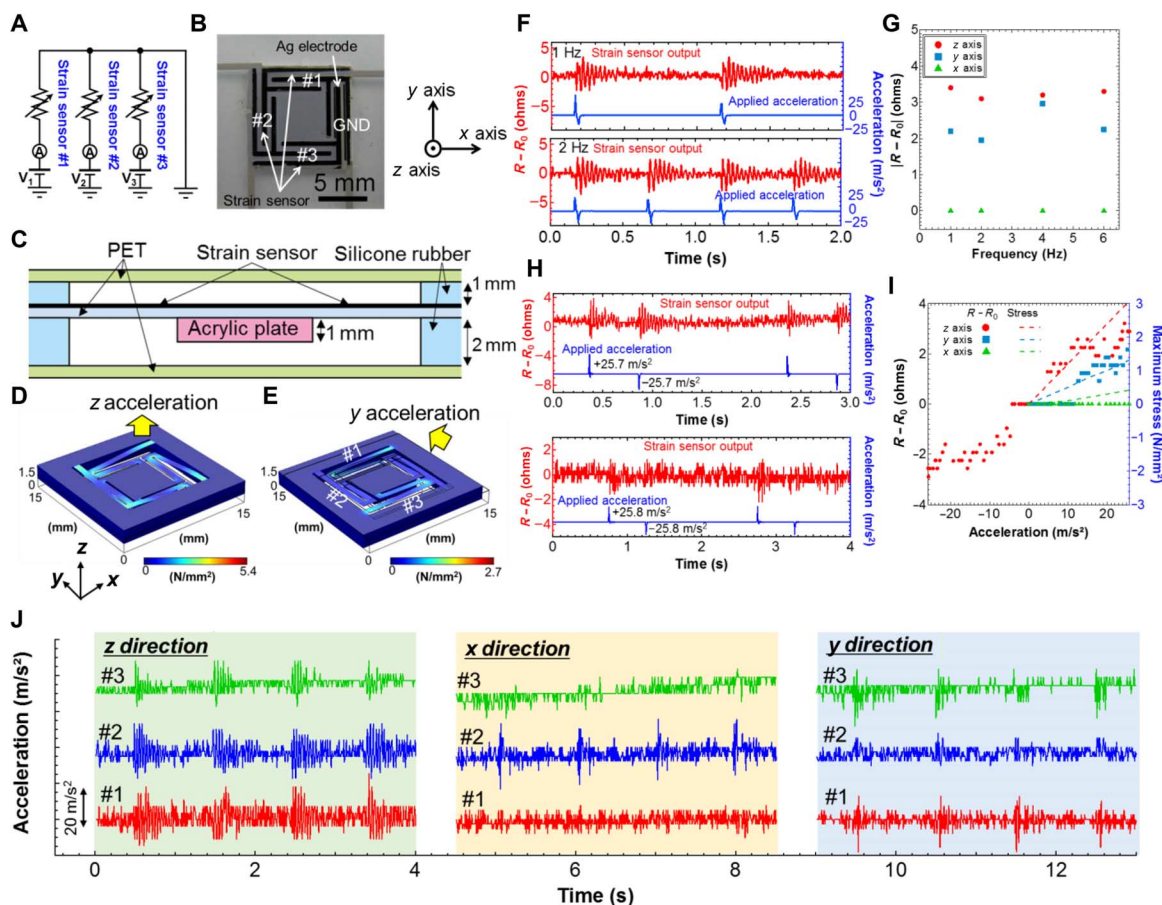
Fig. 2. Printed three-axis acceleration sensor. Circuit diagram (**A**), image (**B**), and cross-sectional schematic (**C**) of the acceleration sensor. GND, ground line. Stress distributions extracted from FEM simulations on application of (**D**) z-axis and (**E**) y-axis accelerations (20 m/s^2). (**F**) Resistance change of strain sensor #1 under z-axis acceleration of 1 and 2 Hz. (**G**) Compiled resistance change of sensor #1 under x-, y-, and z-axis accelerations as a function of acceleration frequency. Resistance change of sensor #1 under y- and z-axis positive and negative accelerations (**H**) and their compiled results, with maximum stress extracted from the FEM simulations (**I**). (**J**) Three-axis acceleration detection by measuring the three strain sensors simultaneously when x-, y-, and z-axis accelerations are applied.

results, the lower limit of stress detection by the sensor should be ~0.6 ± 0.1 N/mm^2. Although this sensitivity is sufficient for monitoring higher-intensity activity, such as walking and running, further improvements should be made to detect lower-intensity activities, for example, movement of an elderly person. These could be achieved by optimizing the sensor materials and device structure. Finally, to demonstrate the operational capability of the sensor, an acceleration of ~20 m/s^2 in x, y, and z directions was applied, and the device response was evaluated by measuring the resistance change of three individual strain sensors simultaneously (sensors #1 to #3, Fig. 2B). The data in Fig. 2J show that the direction of acceleration and strength can be distinguished by reading the difference in output between sensor #1 (or sensor #3) and sensor #2. These results are the first demonstration of a functional, printed acceleration sensor on a flexible substrate. Because only three-axis acceleration can be measured, it can only detect human motions of moving, standing, and lying down. To observe the detailed motions, such as directions of moving and twisting of the body, further axis acceleration sensor to measure rotation and high sensitivity is required. Although the sensor has a low sensitivity and a large size, including thickness, compared to the conventional Si-based acceleration sensor, this demonstration is an important step in realizing a printed sensor network, which allows

it to integrate all sensors using printing methods, including assembly and packaging processes with a low-cost manufacture.

For health monitoring functionality, sensors for the detection of skin temperature, heartbeat, and sunlight exposure were integrated into the device—the first two were fabricated on the disposable sensing sheet, and the last one was fabricated on the reusable component. The temperature and UV sensors were integrated in series with CNT-TFTs, enabling switching of the components, as shown in Fig. 3A. This could be used to reduce power consumption and could be enabled by integrating a shift register and other circuits. The ECG sensor makes contact with the skin through a set of three Ag electrodes printed on the disposable PET sheet, and the ECG signal was monitored using commercially available discrete circuits, which consist of amplifiers and filters (Fig. 3B). To make a good contact between the electrodes and skin, we applied a conductive medical grease. Images of the sensors are presented in Fig. 3 (C to E).

Monitoring of skin temperature was achieved by measuring the characteristics of the CNT-TFT, which controls switching of the temperature sensor. The temperature output was extracted from the I_{DS}-V_{GS} properties (as shown in Fig. 3F), using the on-current values measured at $V_{GS} = -5$ V. The results indicate that the on-current changes as a function of temperature, arising from the resistance
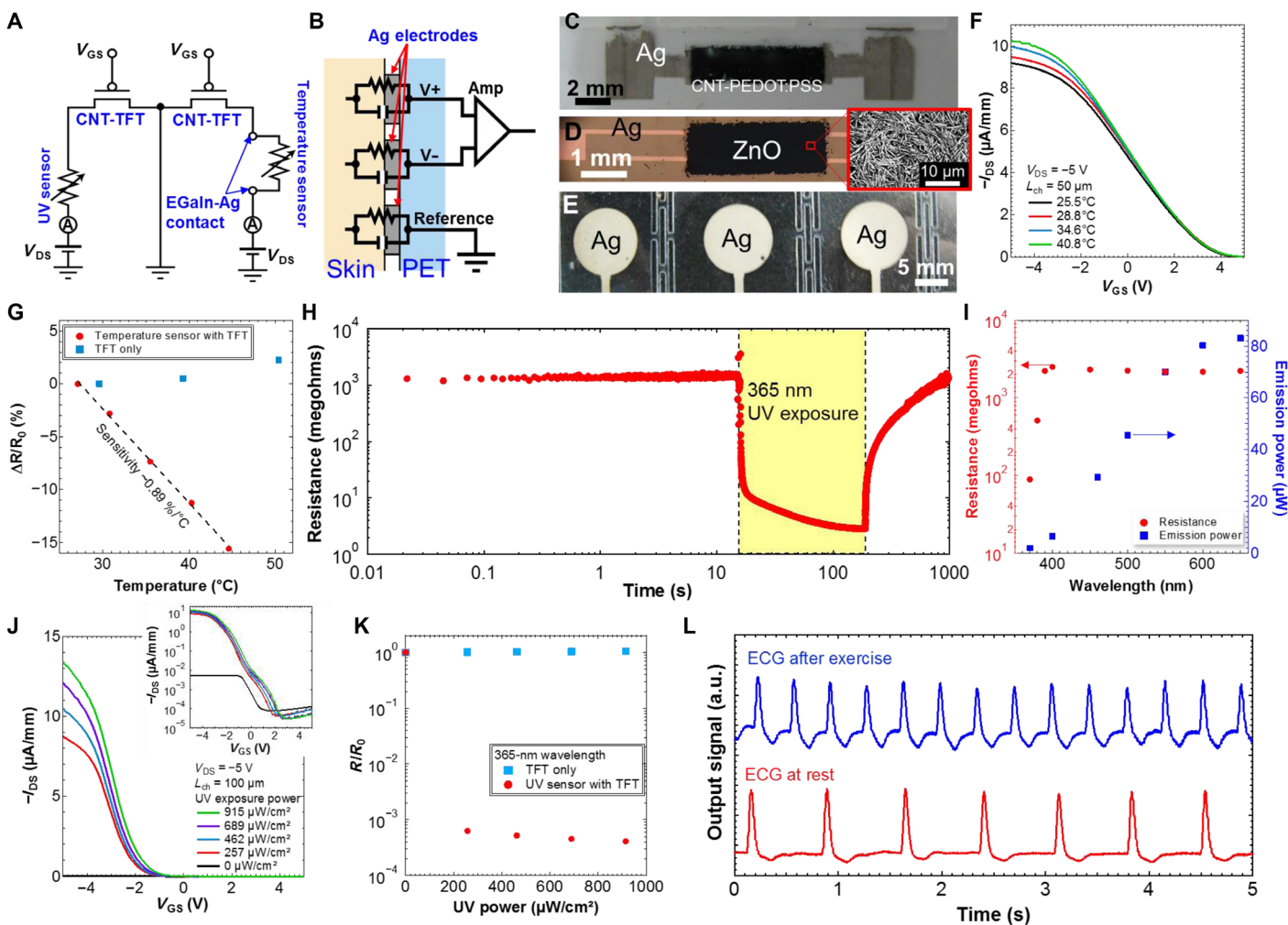
Fig. 3. Multifunction sensors integrated with CNT-TFTs. Circuit diagrams of (**A**) temperature and UV sensors with the intersheet EGaIn-Ag contact and CNT-TFTs and (**B**) ECG sensor. Amp, amplifier. Images of (**C**) temperature sensor, (**D**) UV sensor (with inset magnified scanning electron microscopy image showing the surface of the ZnO nanowire network), and (**E**) ECG sensor. (**F**) I_{DS}-V_{GS} characteristics at $V_{DS} = -5$ V as a function of temperature for CNT-TFT integrated with the temperature sensor. (**G**) Normalized resistance change ($\Delta R/R_0$, $\Delta R = R - R_0$) of on-current at $V_{GS} = -5$ V for CNT-TFTs with and without a temperature sensor, where R and R_0 are the resistances at the measured and room temperatures, respectively. (**H**) Real-time resistance measurement of UV sensor under 365-nm UV exposure. (**I**) Compiled resistance of UV sensor and applied UV irradiation power as a function of wavelength. (**J**) I_{DS}-V_{GS} characteristics at $V_{DS} = -5$ V as a function of UV exposure power for CNT-TFTs integrated with a UV sensor. Inset: Log current of I_{DS}-V_{GS} plot. (**K**) Normalized resistance change (R/R_0) of on-current at $V_{GS} = -5$ V for CNT-TFTs with and without a UV sensor, where and R and R_0 are the resistances with and without UV exposure, respectively. (**L**) Recorded ECG signal after exercise and at rest condition. a.u., arbitrary unit.

change of the temperature sensor. To determine the origins of the on-current change, we analyzed the resistance change ratio, $\Delta R/R_0$ ($\Delta R = R - R_0$), as a function of temperature for TFTs with and without a temperature sensor (Fig. 3G). Here, R is the resistance measured at a given temperature, and R_0 is the resistance value at room temperature. The results indicate that the resistance decreases linearly with increasing temperature, whereas the resistance of the stand-alone CNT-TFT (without the sensor) is almost constant, exhibiting only a very slight resistance increase with temperature. This finding suggests that the resistance change observed in the data in Fig. 3F arises predominantly from the temperature sensor. From these data, the sensitivity of the sensor was calculated to be ~0.89%/°C, a relatively high value, which is attributed to electron hopping at the interface between the CNT and PEDOT:PSS in the temperature sensor (11). In addition to the sensor function, reliability of electrical contact through EGaIn

was also tested by repeating attachments and detachments between layers. Figure S8 indicates that electrical resistance measured at $V_{GS} = -5$ V and $V_{DS} = -1$ V is electrically stable up to at least 70 cycles.

Next, the UV sensor response was characterized by exposure to UV light, with an irradiating power of 689 μW/cm^2 at a wavelength of 365 nm. Figure 3H shows that the resistance drastically decreases by around three orders of magnitude on illumination. The relatively slow response time observed for the device is attributed to the mechanism of oxygen absorption and desorption from ZnO surfaces on exposure to UV light (24, 25). Because multilayered ZnO network film (as shown in Fig. 3D) is used, oxygen absorption and desorption take a long time. Although this is speculation, this phenomenon is confirmed by changing the thickness of ZnO network film between ~3.5 and ~15 μm, as shown in fig. S9, indicating that the response time is slower for thicker ZnO layers. On UV exposure, the resistance

decreased to ~$1/100$ of the original value over the course of 1.3 s, with saturation achieved ~150 s at a resistance of ~$1/1000$. On removal of the UV light source, the sensor resistance returned to the original value after a period of ~730 s. From the results in Fig. 3I, it was also confirmed that the ZnO nanowire UV sensor is sensitive to wavelengths below 390 nm, corresponding to an electronic excitation energy of ~3.2 eV, which is close to the known electronic band gap of ZnO. As with the temperature sensor, the UV sensor was also integrated in series with a CNT-TFT to enable switching. Because of the large resistance change in the sensor on exposure to UV light, the on-current of the connected CNT-TFT changes substantially with different illumination intensity, as shown by the data in Fig. 3J. A comparison between the R/R_0 resistance ratios of the stand-alone CNT-TFT and the UV sensor–integrated TFT shows that the observed sharp resistance change can be attributed almost exclusively to the output from the sensor and that illumination does not significantly alter the characteristics of the stand-alone transistor for short- and long-time exposures (Fig. 3K and fig. S10). Therefore, it may be concluded that the incident UV intensity can be readily derived by measuring the on-current value of the CNT-TFT. For UV detection, it is required to measure the dose amount by monitoring the resistance change by integrating memory functions in the future.

The ECG sensor makes contact directly on the skin via three Ag electrodes, as described in Fig. 3E and fig. S4C. Because of the small magnitude of the ECG signal (a few millivolts) recorded from the skin, several amplifiers and filters were connected to the circuit to amplify the signal and remove high-frequency noise. This circuit is illustrated in Fig. 3B and fig. S11. After the sensor was attached to the body, the ECG signal was monitored, extracting a heart rate value of 82 beats per minute (BPM) at rest and 172 BPM after exercise from the measured output signal, as displayed in the results in Fig. 3L.

Finally, as a first proof of concept of the device's full functionality (that is, flexible attachment to the body, acquisition of multiple sets of health information, and the simultaneous monitoring of physical movement), the device was attached directly onto the skin on the chest of a 23-year-old male. The placement of the device is shown in Fig. 4A. This experiment was carried out indoors, and the output of each sensor was measured simultaneously (fig. S12). Because of limitations in the measurement setup, only one beam, sensor #1, of the acceleration sensor was used to detect movement (that is, detection in the y axis; Fig. 2B). During the test, skin temperature, ECG, and UV exposure were monitored in real time under the following states of physical activity: rest, fast steps (simulating running), walking-pace steps, and lying down (simulating sleeping). The temperature and UV sensors were controlled by switching the CNT-TFTs. For the on-state, a square wave with an amplitude of −3 V and a frequency of 6 Hz was applied to the gate electrodes; for the off-state, the same wave with an amplitude of +3 V was applied. The full set of measurements is shown in Fig. 4B. The skin temperature was around 32°C, whereas the average heart rate derived from the ECG signal was measured to vary between 76.8 BPM at rest and 89.9 BPM, depending on the degree of physical activity, respectively (Fig. 4, C and D). The skin temperature was almost constant because of short measurement time and exercise, which was also confirmed by a commercially available infrared (IR) sensor
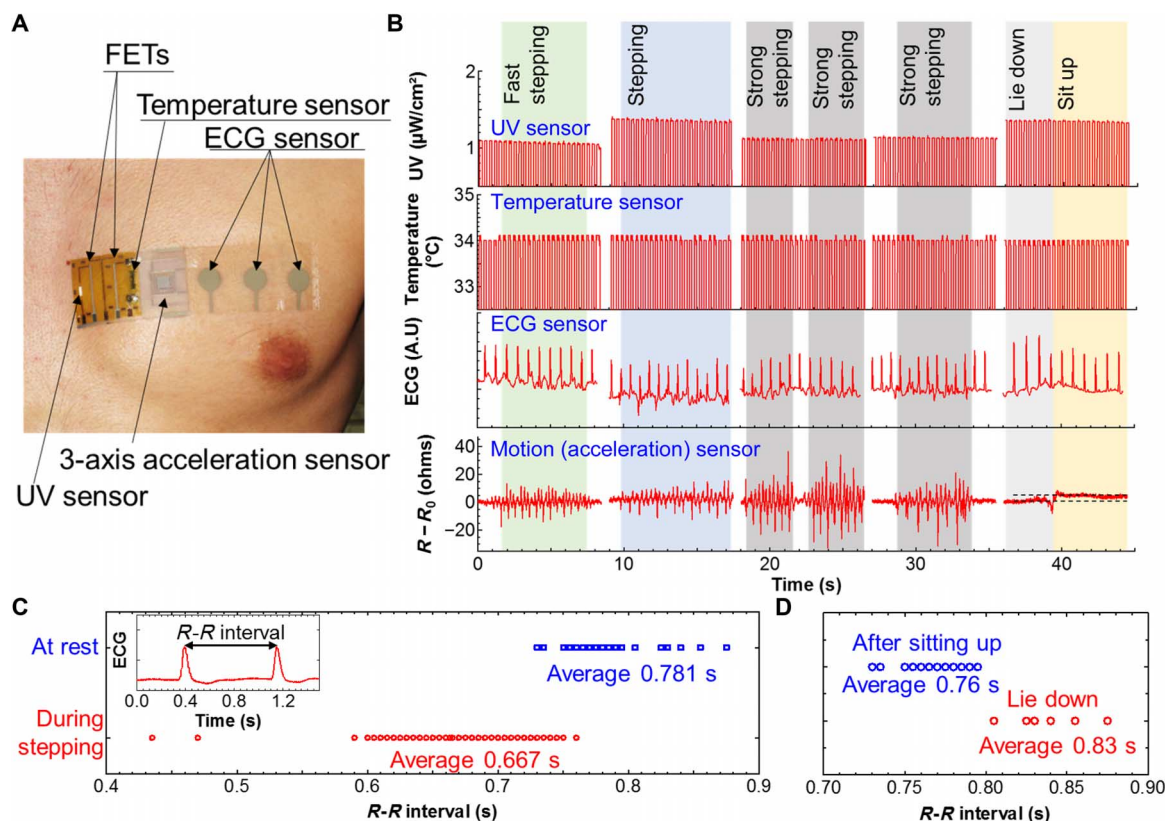

Fig. 4. Proof-of-concept health care monitoring demonstration. (**A**) Image of the multifunctional device attached directly onto the skin. FETs, field-effect transistors. (**B**) Real-time acceleration (motion), ECG, skin temperature, and UV monitoring results. (**C**) R-R intervals at rest and during stepping (activity) measured by the device. Inset: ECG time plot showing method for measuring the R-R interval of the ECG signal. (**D**) R-R intervals at the lie-down state and right after the sitting-up state from the lie-down state.

(fig. S13). As expected, the results show that the measured heart rate strongly depends on the person's motion, emphasizing the importance of monitoring health conditions simultaneously with physical activity. Because the experiments were conducted in a room, the UV exposure was measured to be ~1 μW/cm^2. However, under sunlight, the UV power was increased to around 170 μW/cm^2 (fig. S14). Finally, the acceleration sensor could successfully distinguish between each physical activity, and differentiation between running simulation and walking steps was possible by monitoring the frequency and amplitude of the acceleration peaks. Furthermore, a comparison between the acceleration sensor outputs from lie-down to sit-up states, as shown in Fig. 4B, reveals that the sensor output generates an increase in resistance and no peaks are observed; this is in stark contrast with the output signature obtained for all the states involving movement. This finding suggests that the acceleration sensor can monitor human movements and differentiate between active conditions and passive ones (that is, standing and lying down), and that different states can be identified from the output signature, with the exception of eating/drinking.

Power consumption is also an important factor for the practical application of the device as a total system. The device discussed here has not been integrated with a signal processing system, so we have not measured the power consumption or source; these factors require further study.

DISCUSSION

In conclusion, this study successfully demonstrates the operation of a multifunctional, flexible, wearable health care monitoring device equipped with a movement sensor. This device also demonstrates the effectiveness of using a flexible and stable, low-resistance EGaIn liquid metal contact for the attachment of different device components. Here, the design of a disposable sensing sheet for direct contact with the skin alongside the nondisposable sheet with higher-cost devices demonstrates that this type of architecture offers a wide range of design possibilities. Hence, this concept provides a solid development platform for low-cost flexible electronics in the health care monitoring sector. For an initial proof of concept, we successfully demonstrated simultaneous monitoring of skin temperature, heart rate, and UV light exposure while also monitoring physical activity through an acceleration sensor. Although the device used in this demonstration was not wearable (that is, while the sensing components were mounted on the body, the signal processing circuits and battery were not integrated into the device, which would be required for commercially viable health care monitors), the successful real-time operation of this all-printed device is an important step in the development of flexible electronics not only for health care monitoring but also for macroscale sensor sheets in alternative applications. Furthermore, by combining this technology with flexible chemical sensing functionality reported recently by other groups (8), wearable and flexible smart health care devices could become generally available, useful for a number of purposes, and helpful to a wide range of people.

MATERIALS AND METHODS
Three-axis acceleration sensor
First, an Ag electrode (Asahi Chemical) was screen-printed on a 38-μm-thick PET film. After the Ag ink was cured at 70°C, four beam structures were formed by using a laser cutter tool. Second, strain sensors were printed on the beam structures using CNT ink (SouthWest Nano-

Technologies) and AgNP ink (Paru) with a weight ratio of 5:3, followed by curing at 70°C (26). The sensor film was sandwiched between one 1-mm-thick and one 2-mm-thick silicone rubber film with a hole (Fig. 2C). Finally, 38-μm-thick PET films were applied to the silicone rubber films on both sides of the sensor, rendering the structure mechanically inflexible.

Temperature and ECG sensors
Ag electrodes for the ECG sensor and interconnection with the temperature sensor were printed on a 38-μm-thick PET film. This component was designed to be used as a disposable sheet. After the electrode was cured at 70°C, a mixture of PEDOT:PSS solution (Sigma-Aldrich) and CNT ink (3:1 weight ratio) was printed and cured at 70°C (3).

UV sensor
ZnO nanowires (~90 nm in diameter and ~1 μm in length; Sigma-Aldrich) were dispersed in deionized (DI) water with a weight ratio of 100:1 (DI/ZnO) using a homogenizer for 10 min. The solution was then dropped on the polyimide substrate with CNT-TFTs over a patterned film, followed by curing at 200°C and removing the film. This component was designed to be a nondisposable sensor sheet because it is not intended to be used in contact with the skin.

Carbon nanotube thin-film transistors
For the substrate, an ~10-μm polyimide film was spin-coated onto a Si/SiO$_2$ handling wafer. Subsequently, a 10-nm-thick SiO$_x$ was deposited onto the substrate to act as an adhesion layer between the polymer and the metal layers. The gate electrodes consisted of patterned ~100-nm-thick Al films deposited by sputtering. Then, Cr/Au (5/30 nm) layers were deposited onto the pads of the gate electrode to protect it from an etching process of the dielectric layer. Next, 50-nm-thick Al$_2$O$_3$ and 10-nm-thick SiO$_x$ layers were deposited as the gate dielectric layer by atomic layer deposition (Arradiance) and electron beam evaporation, respectively. For the semiconductor channels, CNT network films were formed using a 99% semiconductor-enriched solution (NanoIntegris) mixed with a sodium cholate surfactant (27) and patterned to form TFT channels using oxygen plasma. Other Cr/Au (5/30 nm) layers were then lifted off to form the source and drain electrodes. The dielectric layer was etched using a buffered hydrogen fluoride solution to open up the contact pads of the gate electrodes. To remove solvent residue from the CNT network, vacuum annealing was conducted at 200°C for 90 min. Polymer resist and PET films were then coated and laminated over the TFTs to protect the devices from scratches and stress caused by bending. Finally, the polyimide film was peeled off from the Si/SiO$_2$ handling wafer.

EGaIn chamber
To create the contact for the reusable polyimide substrate sheet using a laser cutting tool, a 2-mm-diameter hole was made in a 0.5-mm-thick silicone rubber sheet, and a 1-mm-diameter hole was made in a 0.25-mm-thick PDMS sheet, forming the chamber and ejection holes, respectively. These two sheets were then laminated using an adhesive tape. After alignment between the holes and the electrodes on the polyimide film, these sheets were also laminated. Finally, these holes in the silicone rubber/PDMS sheet were filled with the EGaIn liquid metal (fig. S3).

Device assembly
After the components were fabricated, they were assembled for the multifunctional health care device. The final device structure is shown

in fig. S1. First, the acceleration sensor was attached on a PET film using a double-sided tape, where temperature and ECG sensors were integrated. Second, for reusable sheets integrated with CNT-TFTs, UV sensor, and EGaIn electrode, because of good adhesion between PDMS and PET films, the reusable sheets can be attached onto the PET film without using any glue or tape. Finally, to place the device on skin, we used a double-sided tape. The double-sided tape was not confirmed as a biocompatible material because this study focuses on the demonstration of a proof of concept of health condition sensing. This adhesion needs to be explored further in the future for the practical use of wearable devices.

SUPPLEMENTARY MATERIALS

Supplementary material for this article is available at http://advances.sciencemag.org/cgi/content/full/2/11/e1601473/DC1

fig. S1. Cross-sectional device schematic image.
fig. S2. Electrical resistance change of Ag electrodes over the kirigami structure.
fig. S3. Schematic image of reusable and disposable sensor sheets.
fig. S4. Images of disposable and reusable sensor sheets.
fig. S5. Electrical stability of EGaIn and Ag contact under motion.
fig. S6. FEM simulation.
fig. S7. Frequency dependence of three-axis acceleration sensor.
fig. S8. Cycle test of electrical contacts between EGaIn and Ag electrodes.
fig. S9. Thickness dependence of UV sensors.
fig. S10. TFT characteristics under UV exposure.
fig. S11. Circuit diagram of ECG recording.
fig. S12. Measurement setup.
fig. S13. Skin temperature measurements using the printed temperature sensor and an IR sensor.
fig. S14. UV detection under simulated sunlight.

REFERENCES AND NOTES

1. K. Takei, W. Honda, S. Harada, T. Arie, S. Akita, Toward flexible and wearable human-interactive health-monitoring devices. *Adv. Healthcare Mater.* 4, 487–500 (2015).
2. T. Yokota, Y. Inoue, Y. Terakawa, J. Reeder, M. Kaltenbrunner, T. Ware, K. Yang, K. Mabuchi, T. Murakawa, M. Sekino, W. Voit, T. Sekitani, T. Someya, Ultraflexible, large-area, physiological temperature sensors for multipoint measurements. *Proc. Natl. Acad. Sci. U.S.A.* 112, 14533–14538 (2015).
3. K. Kanao, S. Harada, Y. Yamamoto, W. Honda, T. Arie, S. Akita, K. Takei, Highly selective flexible tactile strain and temperature sensors against substrate bending for an artificial skin. *RSC Adv.* 5, 30170–30174 (2015).
4. T. Kim, J. Park, J. Sohn, D. Cho, S. Jeon, Bioinspired, highly stretchable, and conductive dry adhesives based on 1D–2D hybrid carbon nanocomposites for all-in-one ECG electrodes. *ACS Nano* 10, 4770–4778 (2016).
5. J.-W. Jeong, M. K. Kim, H. Cheng, W.-H. Yeo, X. Huang, Y. Liu, Y. Zhang, Y. Huang, J. A. Rogers, Capacitive epidermal electronics for electrically safe, long-term electrophysiological measurements. *Adv. Healthcare Mater.* 3, 642–648 (2014).
6. G. Schwartz, B. C.-K. Tee, J. Mei, A. L. Appleton, D. H. Kim, H. Wang, Z. Bao, Flexible polymer transistors with high pressure sensitivity for application in electronic skin and health monitoring. *Nat. Commun.* 4, 1859 (2013).
7. Y. Zang, F. Zhang, D. Huang, X. Gao, C.-a. Di, D. Zhu, Flexible suspended gate organic thin-film transistors for ultra-sensitive pressure detection. *Nat. Commun.* 6, 6269 (2015).
8. H. Lee, T. K. Choi, Y. B. Lee, H. R. Cho, R. Ghaffari, L. Wang, H. J. Choi, T. D. Chung, N. Lu, T. Hyeon, S. H. Choi, D.-H. Kim, A graphene-based electrochemical device with thermoresponsive microneedles for diabetes monitoring and therapy. *Nat. Nanotechnol.* 11, 566–572 (2016).
9. W. Gao, S. Emaminejad, H. Y. Y. Nyein, S. Challa, K. Chen, A. Peck, H. M. Fadah, H. Ota, H. Shiraki, D. Kiriya, D.-H. Lien, G. A. Brooks, R. W. Davis, A. Javey, Fully integrated wearable sensor arrays for multiplexed in situ perspiration analysis. *Nature* 529, 509–514 (2016).
10. D. Son, J. Lee, S. Qiao, R. Ghaffari, J. Kim, J. E. Lee, C. Song, S. J. Kim, D. J. Lee, S. W. Jun, S. Yang, M. Park, J. Shin, K. Do, M. Lee, K. Kang, C. S. Hwang, N. Lu, T. Hyeon, D.-H. Kim, Multifunctional wearable devices for diagnosis and therapy of movement disorders. *Nat. Nanotechnol.* 9, 397–404 (2014).
11. W. Honda, S. Harada, T. Arie, S. Akita, K. Takei, Wearable, human-interactive, health-monitoring, wireless devices fabricated by macroscale printing techniques. *Adv. Funct. Mater.* 24, 3299–3304 (2014).
12. J. Park, M. Kim, Y. Lee, H. S. Lee, H. Ko, Fingertip skin–inspired microstructured ferroelectric skins discriminate static/dynamic pressure and temperature stimuli. *Sci. Adv.* 1, e1500661 (2015).
13. D.-H. Kim, N. Lu, R. Ghaffari, Y.-S. Kim, S. P. Lee, L. Xu, J. Wu, R.-H. Kim, J. Song, Z. Liu, J. Viventi, B. de Graff, B. Elolampi, M. Mansour, M. J. Slepian, S. Hwang, J. D. Moss, S.-M. Won, Y. Huang, B. Litt, J. A. Rogers, Materials for multifunctional balloon catheters with capabilities in cardiac electrophysiological mapping and ablation therapy. *Nat. Mater.* 10, 316–323 (2011).
14. D.-H. Kim, N. Lu, R. Ma, Y.-S. Kim, R.-H. Kim, S. Wang, J. Wu, S. M. Won, H. Tao, A. Islam, K. J. Yu, T.-i. Kim, R. Chowdhury, M. Ying, L. Xu, M. Li, H.-J. Chung, H. Keum, M. McCormick, P. Liu, Y.-W. Zhang, F. G. Omenetto, Y. Huang, T. Coleman, J. A. Rogers, Epidermal electronics. *Science* 333, 838–843 (2011).
15. K.-I. Jang, S. Y. Han, S. Xu, K. E. Mathewson, Y. Zhang, J.-W. Jeong, G.-T. Kim, R. C. Webb, J. Woo Lee, T. J. Dawidczyk, R. H. Kim, Y. M. Song, W.-H. Yeo, S. Kim, H. Cheng, S. I. Rhee, J. Chung, B. Kim, H. U. Chung, D. Lee, Y. Yang, M. Cho, J. G. Gaspar, R. Carbonari, M. Fabiani, G. Gratton, Y. Huang, J. A. Rogers, Rugged and breathable forms of stretchable electronics with adherent composite substrates for transcutaneous monitoring. *Nat. Commun.* 5, 4779 (2014).
16. W. Honda, High-performance, mechanically flexible, and vertically integrated 3D carbon nanotube and InGaZnO complementary circuits with a temperature sensor. *Adv. Mater.* 27, 4674–4680 (2015).
17. T. Yamada, Y. Hayamizu, Y. Yamamoto, Y. Yomogida, A. Izadi-Najafabadi, D. N. Futaba, K. Hata, A stretchable carbon nanotube strain sensor for human-motion detection. *Nat. Nanotechnol.* 6, 296–301 (2011).
18. B.-C. Zhang, H. Wang, Y. Zhao, F. Li, X.-M. Ou, B.-Q. Sun, X.-H. Zhang, Large-scale assembly of highly sensitive Si-based flexible strain sensors for human motion monitoring. *Nanoscale* 8, 2123–2128 (2016).
19. S. Harada, T. Arie, S. Akita, K. Takei, Highly stable liquid–solid metal contact toward multilayered detachable flexible devices. *Adv. Electron. Mater.* 1, 1500080 (2015).
20. S. Lee, J. Ha, S. Jo, J. Choi, T. Song, W. Il Park, J. A. Rogers, U. Paik, LEGO-like assembly of peelable, deformable components for integrated devices. *NPG Asia Mater.* 5, e66 (2013).
21. M. D. Dickey, R. C. Chiechi, R. J. Larsen, E. A. Weiss, D. A. Weitz, G. M. Whitesides, Eutectic gallium-indium (EGaIn): A liquid metal alloy for the formation of stable structures in microchannels at room temperature. *Adv. Funct. Mater.* 18, 1097–1104 (2008).
22. T. C. Shyu, P. F. Damasceno, P. M. Dodd, A. Lamoureux, L. Xu, M. Shlian, M. Shtein, S. C. Glotzer, N. A. Kotov, A kirigami approach to engineering elasticity in nanocomposites through patterned defects. *Nat. Mater.* 14, 785–789 (2015).
23. T. Takahashi, K. Takei, A. G. Gillies, R. S. Fearing, A. Javey, Carbon nanotube active-matrix backplanes for conformal electronics and sensors. *Nano Lett.* 11, 5408–5413 (2011).
24. C. Soci, A. Zhang, B. Xiang, S. A. Dayeh, D. P. R. Aplin, J. Park, X. Y. Bao, Y. H. Lo, D. Wang, ZnO nanowire UV photodetectors with high internal gain. *Nano Lett.* 7, 1003–1009 (2007).
25. J. Zhou, Y. Gu, Y. Hu, W. Mai, P.-H. Yeh, G. Bao, A. K. Sood, D. L. Polla, Z. L. Wang, Gigantic enhancement in response and reset time of ZnO UV nanosensor by utilizing Schottky contact and surface functionalization. *Appl. Phys. Lett.* 94, 191103 (2009).
26. S. Harada, W. Honda, T. Arie, S. Akita, K. Takei, Fully printed, highly sensitive multifunctional artificial electronic whisker arrays integrated with strain and temperature sensors *ACS Nano* 8, 3921–3927 (2014).
27. D. Kiriya, K. Chen, H. Ota, Y. Lin, P. Zhao, Z. Yu, T.-j. Ha, A. Javey, Design of surfactant–substrate interactions for roll-to-roll assembly of carbon nanotubes for thin-film transistors. *J. Am. Chem. Soc.* 136, 11188–11194 (2014).